Volume 203 July 2013 ISSN 0022-4596

ELSEVIER

JOURNAL OF SOLID STATE CHEMISTRY

IN THIS ISSUE:

Hydrothermal synthesis and structural analysis of new mixed oxyanion borates: $Ba_{11}B_{26}O_{44}(PO_4)_2(OH)_6$, $Li_9BaB_{15}O_{27}(CO_3)$ and $Ba_3Si_2B_6O_{16}$

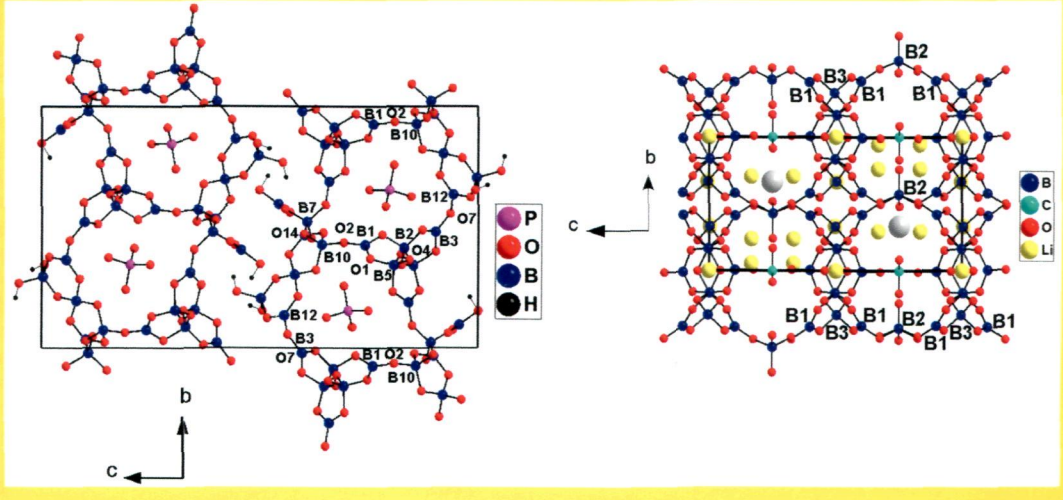

Carla Heyward, Colin D. McMillen and Joseph Kolis

ELSEVIER

Volume 203, July 2013

JOURNAL OF SOLID STATE CHEMISTRY

www.elsevier.com/locate/jssc

CONTENTS

Abstracted/indexed in BioEngineering Abstracts, Chemical Abstracts, Coal Abstracts, Current Contents/Physics, Chemical, & Earth Sciences, Engineering Index, Research Alert, SCISEARCH, Science Abstracts, and Science Citation Index. Also covered in the abstract and citation database SciVerse SCOPUS®. Full text available on SciVerse ScienceDirect®.

Regular Articles

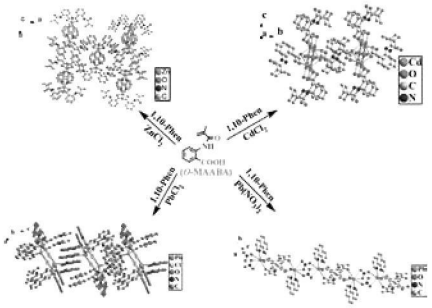

Four coordination compounds constructed by *o*-methacrylamidobenzoic, phenanthroline and metal ions are reported. The photoluminescent properties is studied, which is affected by the molecular stacking and LMCT.

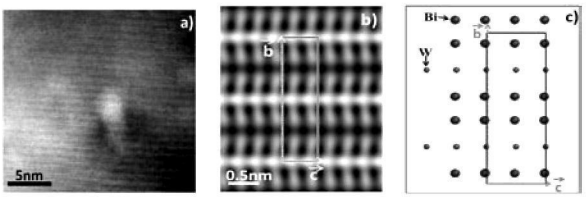

High resolution transmission electron microscopy: inverse fast Fourier transform giving the layered structure of the Bi_2WO_6 phase, with a representation of the cell dimensions (*b* and *c* vectors). The $Bi_2O_2^{2+}$ and WO_4^{2-} sandwiches are visible in the IFFT image.

Regular Articles—Continued

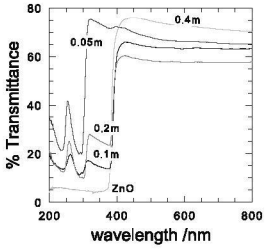

The phenomenon indicates that the optical energy gap is enlarged with the increase of molar concentrations in 2,4-dichlorophenoxy acetate anion content into ZnO to create a ZLH–24D nanohybrid

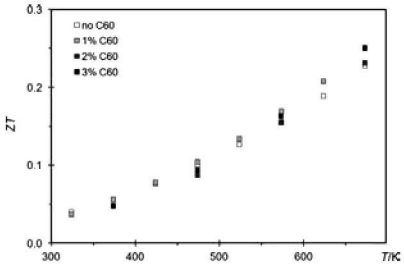

Figure-of-merit of various $Ni_{0.05}Mo_3Sb_{5.4}Te_{1.6}$/C composites.

Continued

Synthesis and single-crystal structure determination of the zinc nitride halides Zn_2NX (X = Cl, Br, I)

Xiaohui Liu, Claudia Wessel, Fangfang Pan, Richard Dronskowski

page 31

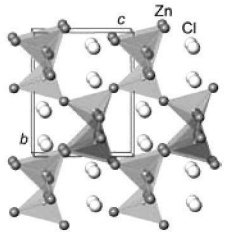

Zn_2NCl, Zn_2NBr, and Zn_2NI have been synthesized, and their crystal structures (Cl and Br phases: *Pna*2_1; I phase: *Pnma*) have been determined from XRD; the direct band gap of Zn_2NCl is theoretically (HSE06 hybrid functional) predicted as 3.7 eV.

From spin induced ferroelectricity to spin and dipolar glass in a triangular lattice: The $CuCr_{1-x}V_xO_2$ ($0 \leq x \leq 0.5$) delafossite

S. Kumar, K. Singh, M. Miclau, Ch. Simon, C. Martin, A. Maignan

page 37

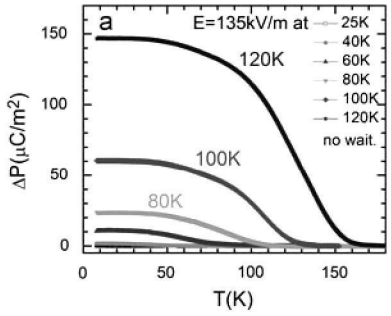

The P(T) curves evidencing the aging effect on polarization in $CuCr_{0.5}V_{0.5}O_2$: $E = 135$ kV/m is applied during cooling at different temperatures. The P values and the inflection point of the transition depend on the poling temperature suggesting a relaxor behaviour. This effect related to the spin glass state is not observed for the lowest vanadium content.

Self-assembled cabbage-like $NaInS_2$ microstructures with efficient visible light photocatalytic performance

Yuanhao Gao, Xuezhen Zhai, Yange Zhang, Zhihong Xu, Pinjiang Li, Zhi Zheng

page 44

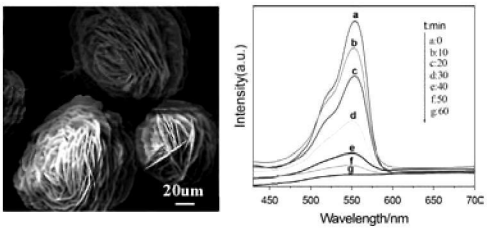

Cabbage-like $NaInS_2$ microstructures were facilely synthesized *via* simple hydrothermal reaction. The cabbage-like $NaInS_2$ architectures exhibit the superiority of photocatalytic performance for the photodegradation of RhB irradiation under visible light irradiation.

Investigation of an unusual low-temperature phase transformation in $RbBH_4$ by neutron diffraction

Brian B. Kitchen, Nina Verdal, Terrence J. Udovic, John J. Rush, Michael R. Hartman, Daniel J. DeVries

page 51

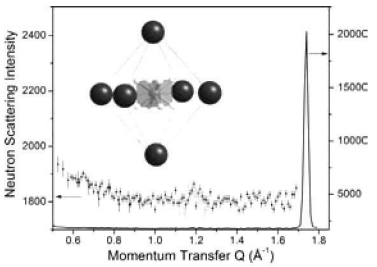

The neutron powder diffraction pattern of $RbBD_4$ below the phase transition temperature (shown here in black) is indistinguishable from that collected above the phase transition temperature. The inset depicts the cubic structure that fits the data at both temperatures.

Effect of co-doping Tm^{3+} ions on the emission properties of Dy^{3+} ions in tellurite glasses

T. Sasikala, L. Rama Moorthy, A. Mohan Babu, T. Srinivasa Rao

page 55

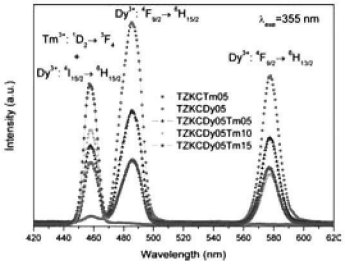

The graphical abstract shows the emission spectra of Dy^{3+}, Tm^{3+} and Dy^{3+}/Tm^{3+} co-doped TZKC glasses recorded by exciting at 355 nm wavelength.

Facile approach to prepare hollow coreshell NiO microspherers for supercapacitor electrodes

Dandan Han, Pengcheng Xu, Xiaoyan Jing, Jun Wang, Dalei Song, Jingyuan Liu, Milin Zhang

page 60

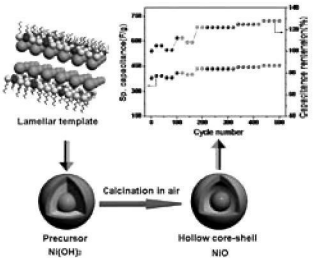

The hollow coreshell NiO was prepared with a facile lamellar template method. The prepared NiO show higher capacitance, lower ion diffusion resistance and better electroactive surface utilization for Faradaic reactions.

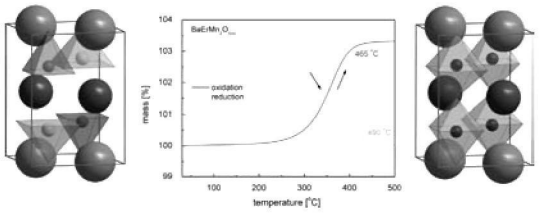

Structure and oxygen storage properties of $BaErMn_2O_{5+\delta}$.

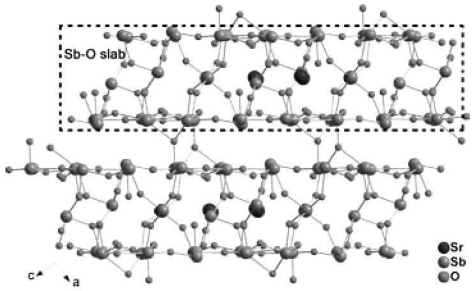

The 2D SbO slabs are stacked through sharing oxygen atoms to form the 3D network structure of the new strontium antimonate^{III} $Sr_5Sb_{22}O_{38}$.

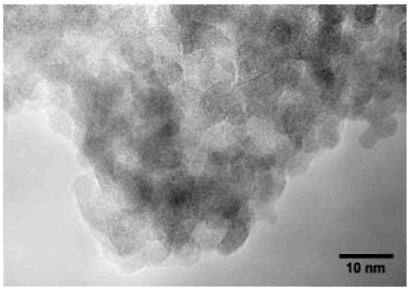

Mesoporous amorphous phase with a high surface area of titania zirconia mixed oxide obtained by hydrothermal preparation.

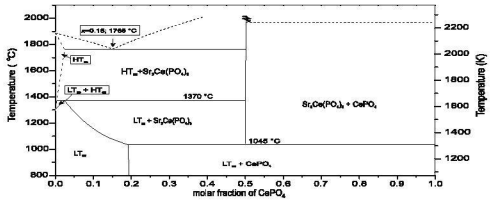

The phase diagram of $Sr_3(PO_4)_2CePO_4$ system showing the stability ranges of limited solid solution and $Sr_3Ce(PO_4)_3$ phases.

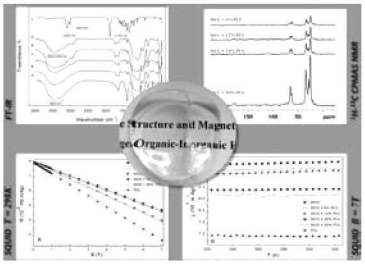

Characterization and magnetic properties of SiO_2/PCL organic–inorganic hybrid materials synthesized via solgel. FT-IR, Fourier transform infrared spectroscopy; solid-state NMR: solid-state nuclear magnetic resonance; SQUID: superconducting quantum interference device.

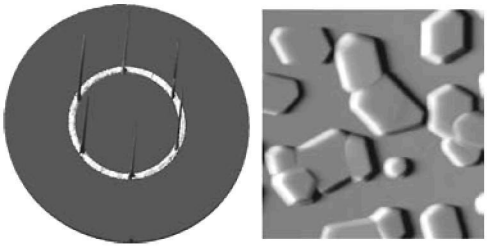

XRD pole figure and AFM patterns of $Ba_2Zn_2Fe_{12}O_{22}$ thin film epitaxially grown on $SrTiO_3$(1 1 1) single crystal using seeding layer templating.

Continued

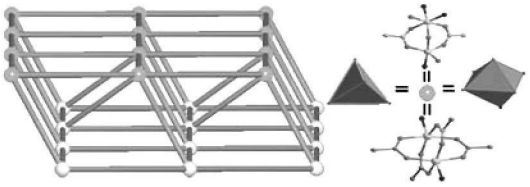

Diverse assemblies of the (4,4) grid layers with different network nodes forms five coordination polymers that are well characterized by IR, TGA, element analysis, fluorescent and magnetic measurement.

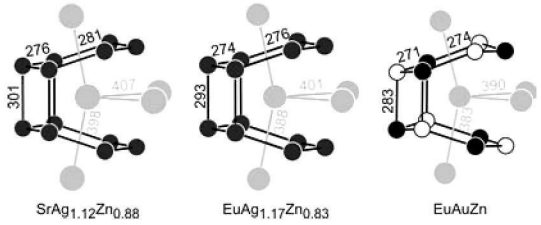

The near neighbor coordination of the strontium and europium atoms in $SrAg_{1.12}Zn_{0.88}$, $EuAg_{1.17}Zn_{0.83}$, and EuAuZn.

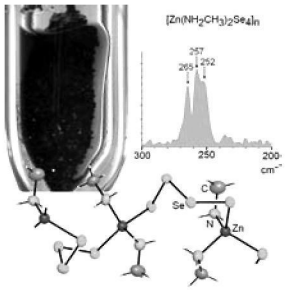

The reaction of Zn and Se in liquid methylamine yields dark red $[Zn(NH_2CH_3)Se_4]$, a 1D coordination polymer consisting of helical Zn–Se_4–Zn– chains.

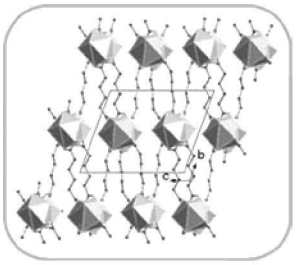

A survey of structures and topologies of lanthanide adipate compounds is presented. A newly synthesized lanthanium adipate complex $\{[La_2(adip)_3(H_2O)_2]$ ($adipH_2$ = adipic acid) is also reported.

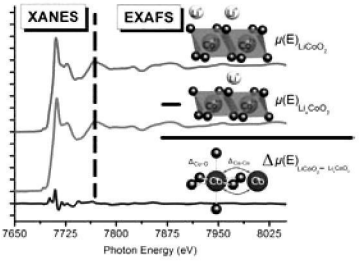

Electrochemical cycling of Li-ion batteries has strong impact on the structure and integrity of the cathode active material particularly near the surface/electrolyte interface. In developing a new method, we have used *in-situ* X-ray absorption spectroscopy during electrochemical cycling of nanoscale $LiCoO_2$ to track changes during charge and discharge and between subsequent cycles. Using difference spectra, several small changes in Co-O bond length, Co-O and Co-Co coordination, and site exchange between Co and Li sites can be tracked. These methods show promise as a new technique to better understand processes which lead to capacity fade and loss in Li-ion batteries.

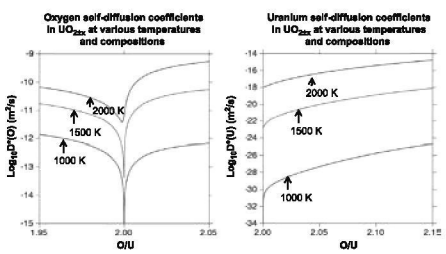

Complete description of OxygenUranium diffusion as a function of composition at various temperatures according to the developed Dictra model.

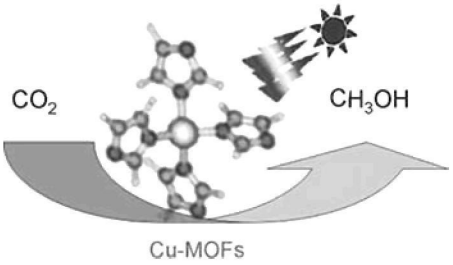

Carbon dioxide was reduced into methanol with water over copper (II) imidazolate frameworks under visible light irradiation.

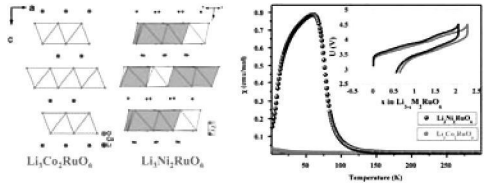

Two new rock salt related oxides of formula, $Li_3M_2RuO_6$, (M = Co, Ni) have been prepared. The M = Co oxide adopts the $LiCoO_2$ (R-3m) structure and the M = Ni oxide adopts a similar layered structure related to Li_2TiO_3, monoclinic ($C2/c$), with partial mixing of Li and Ni/Ru atoms. For $Li_3Co_2RuO_6$, oxidation state for Ru is 4+ and antiferromagnetic (AFM) order is found below 10 K while for the analogous $Li_3Ni_2RuO_6$, Ru oxidation state is 5+ and a ferrimagnetic (FM) behavior with a Curie temperature of 100 K is found. Electrochemical studies correlate well with both magnetic properties and crystal structure.

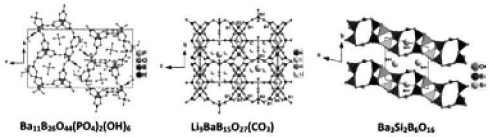

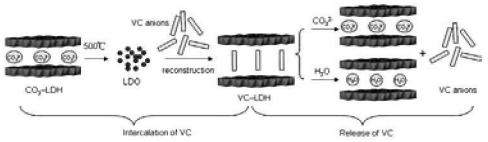

Vitamin C anions have been intercalated in the interlayer space of layered double hydroxide and released in CO_3^{2-} solution and deionised water.

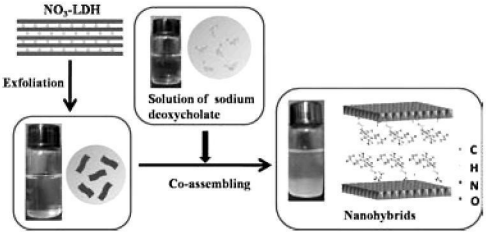

Deoxycholate intercalated layered double hydroxide nanohybrids were successfully synthesized via a coassembly strategy. In this strategy, the interlayer spaces of LDHs can be efficiently used for the intercalation of guest species.

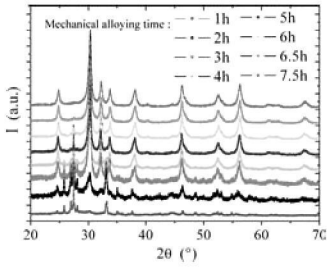

BiCuSeO synthesis by mechanical alloying: phase pure after 7.5h.

Continued

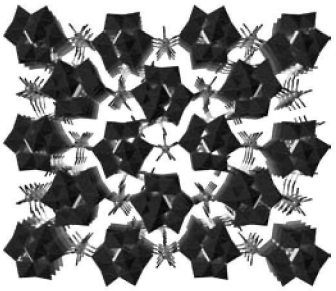

A series of lanthanide-substituted polyoxometaloaluminates have been hydrothermally made and their photoluminescence, nonlinear optical and ferroelectricity properties have also been investigated, respectively.

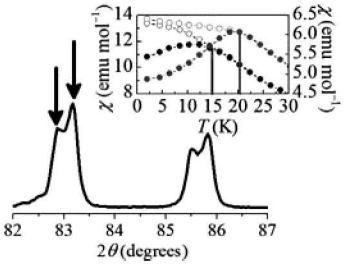

The cubic $Lu_2Mo_2O_{7-x}$ system exhibits a miscibility gap between coexisting pyrochlore phases at 1600 °C. Neutron powder diffraction refinement and chemical analysis shows that the gap separates stoichiometric $x = 0$ and oxygen-deficient $x \approx 0.4$ phases. $Lu_2Mo_2O_{7-x}$ has a frustrated spin glass ground state that is sensitive to the oxygen content.

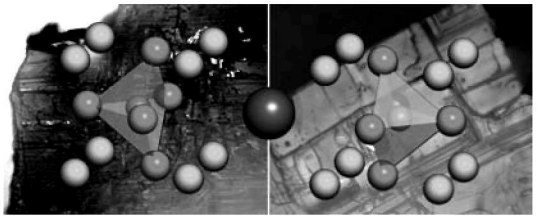

Optical images of $Ba_3Yb_2O_5Te$ in transmission (left) and reflected (right) light, with atomic unit cell overlay.

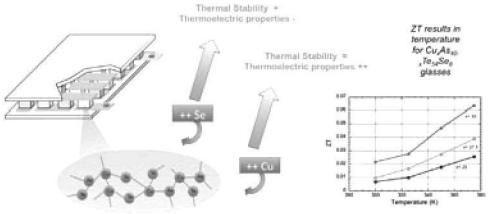

Effect of substitution of Te by Se and As by Cu on thermal stability and thermoelectric properties of $Cu_xAs_{40-x}Te_{60-y}Se_y$ semiconducting glasses.

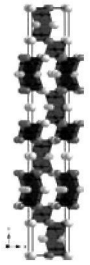

The crystal and magnetic structure of the perovskite phase 15R-$BaFeO_2F$.

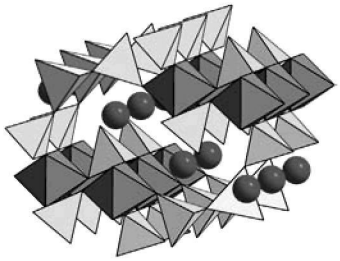

Exploring the Li_2MoO_4–Rb_2MoO_4–$Fe_2(MoO_4)_3$ system showed its partial non-quasiternarity and revealed a new compound $LiRb_2Fe(MoO_4)_3$ which was structurally studied.

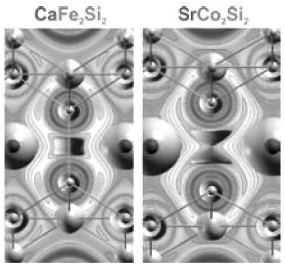

The $SrCo_2Si_2$ and $CaFe_{2-x}Rh_xSi_2$ ($x = 0$, 1.32, and 2) crystallize in the $ThCr_2Si_2$-type. The structure of $SrCo_2Si_2$ contains isolated $[Co_2Si_2]^{2-}$ layers in the *ab*-plane, whereas the $[T_2Si_2]$ layers in $CaFe_{2-x}Rh_xSi_2$ are interconnected along the *c*-axis via Si–Si bonds resulting in a $[T_2Si_2]^{2-}$ network.

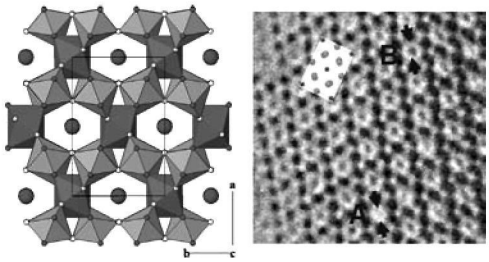

The structure of $RE_xTa_2O_{5+1.5x}$ and its HRTEM image ("A" arrows show empty channel, "B" arrows show filled channel).

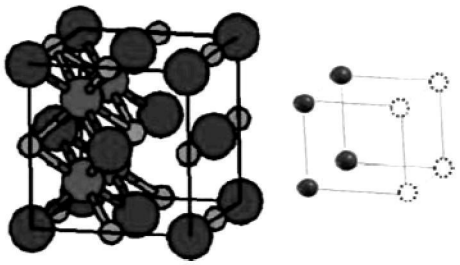

Phase separation and antisite defects in the thermoelectric TiNiSn alloy, are covered as methods for nanostructuring and thereby enhancement of the thermoelectric potential.

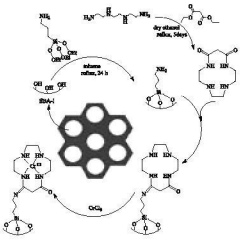

Chromium (III) tetraaza dioxo ligand was grafted onto functionalized SBA-15 using coordinating ability of anchored amino functionalized SBA-15. Preparation of the catalyst is depicted in Scheme 1.

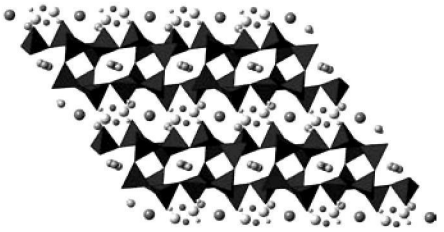

Projection onto (010) of the structure of the natural nanoporous sheet silicate $Na_2CaCu_2Si_8O_{20} \cdot H_2O$ showing the double sheet of corner-linked SiO_4 tetrahedra, intralayer Na and interlayer Na, Ca Cu and H_2O. Small green sphere Cu, large blue spheres Ca, orange purple and yellow small spheres Na, large grey sphere H_2O molecules. Bonds from inter/intralayer species to sheets have been omitted for clarity.

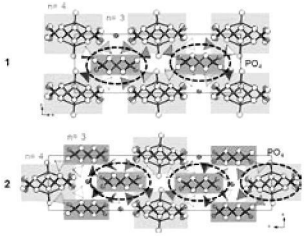

This paper reports the crystal structure of two new bismuth oxophosphate compounds. Both are built on the association of n = 3 and 4 building unit ribbons surrounded by isolated PO4 tetrahedra and tunnels hosting Cu^{2+} cations. They come in addition to the numerous Bi-based compounds already pointed out. Once more, this is the proof of the richness of this crystal system.

Continued

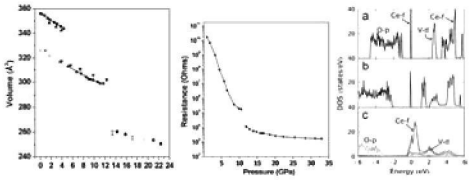

Pressure induced structural phase transition in $CeVO_4$ as observed by x-ray diffraction (pressure vs. volume) and possible metallization in $CeVO_4$ through electrical resistance and first principles electronic structure calculations.

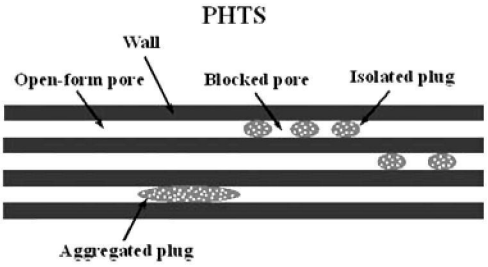

The plugs-containing structures can be interpreted as the distribution of individual isolated plugs along the mesoporous channel.

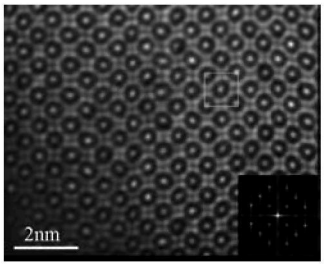

HAADF image for melilite composition $[Nd_{1.5}Ca_{0.5}]_2[Ga]_2[Ga_2O_{7.25}]_2$.

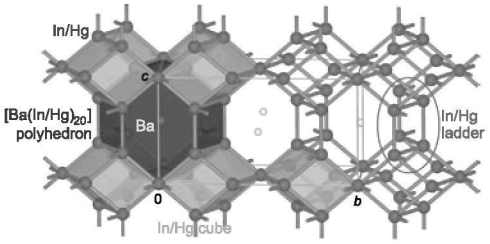

$BaIn_{2.6}Hg_{4.4}$: distorted cubes $[(In/Hg)_8]$ (green, like in $BaHg_{11}$), folded ladders (violet, like in BaIn, $BaHg_2$ and $BaIn_2$) and Ba coordination polyhedra $[Ba(In/Hg)_{20}]$ (blue, like in $BaHg_{11}$).

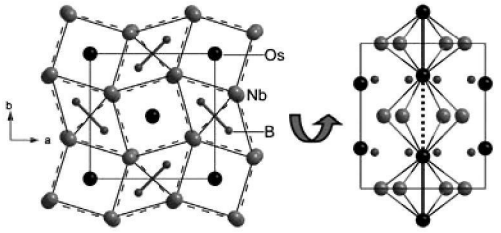

Nb_2OsB_2 is, to the best of our knowledge, the first fully characterized phase in the ternary Nb–Os–B system. It crystallizes (space group *P4/mnc*, 128) with a new twofold superstructure of the U_3Si_2 structure type (space group *P4/mbm*, 127), and is therefore the first boride in this structure family crystallizing with a superstructure of the U_3Si_2 structure type. We show that the distortions leading to this superstructure occurs mainly in the Nb-layer, which tries to accommodate the large osmium atoms. The consequence of this puckering is the building osmium dumbbells instead of chains along [001].

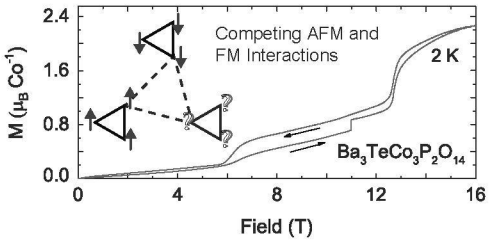

$Ba_3TeCo_3P_2O_{14}$, $Pb_3TeCo_3P_2O_{14}$ and $Pb_3TeCo_3V_2O_{14}$ exhibit a triangles-of-triangles arrangement of the magnetic cations. Despite the Pb-induced crystallographic distortion, all of these materials exhibit competing antiferromagnetic and ferromagnetic interactions that lead to complex high field magnetism.

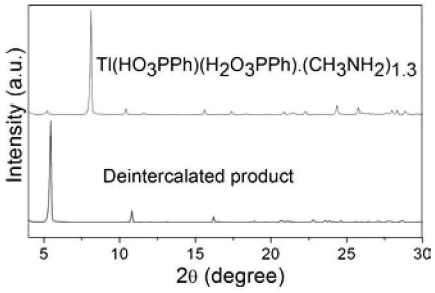

Amongst $A(HO_3PPh)(H_2O_3PPh)$ (A = alkali metal, Tl) phenylphosphonates of four structure types, lithium, sodium, potassium and thallium compounds undergo methylamine intercalation.

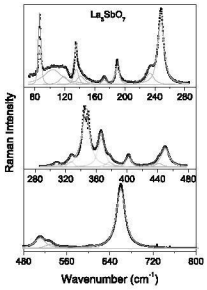

Raman spectrum for La_3SbO_7 ceramics showing their 22 phonon modes adjusted through Lorentzian lines. According to synchrotron X-ray diffraction and Raman scattering, this material belongs to the space group *Cmcm*.

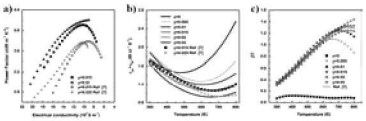

(a) The relationship between electrical conductivity and power factor for Sb/Bi-doped $Mg_{2.16}(Si_{0.4}Sn_{0.6})_{1-y}(Sb/Bi)_y$ ($0 < y = 0.03$) solid solutions.
(b) The correlation between temperature and the combination of the lattice and the bipolar terms of thermal conductivity of $Mg_{2.16}(Si_{0.4}Sn_{0.6})_{1-y}Bi_y$ ($0 = y = 0.03$) solid solutions.
(c) Temperature dependent dimensionless figure of merit ZT of $Mg_{2.16}(Si_{0.4}Sn_{0.6})_{1-y}Bi_y$ ($0 = y = 0.03$) solid solutions.

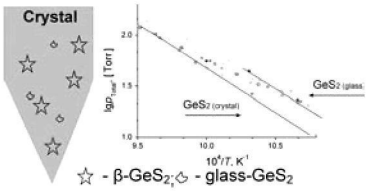

lg $p-1/T$ dependences of as-grown $AgGaGeS_4 \cdot nGeS_2$ crystals.

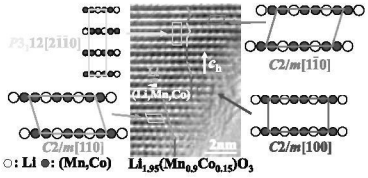

An HREM image for $Li_{1.95}(Mn_{0.9}Co_{0.15})O_3$ and schematic drawings of $C2/m$ and $P3_112$ Li_2MnO_3 projected along the various zone axes. Each projected unit cell is indicated by rectangles and parallelograms

Corrigendum

Language services. Authors who require information about language editing and copyediting services pre- and post-submission please visit http://www.elsevier.com/locate/languagepolishing or our customer support site at http://epsupport.elsevier.com. Please note Elsevier neither endorses nor takes responsibility for any products, goods or services offered by outside vendors through our services or in any advertising. For more information please refer to our Terms & Conditions http://www.elsevier.com/termsandconditions

For a full and complete Guide for Authors, please go to: http://www.elsevier.com/locate/jssc

Journal of Solid State Chemistry has no page charges.